

Low-complexity modulation format identification based on am- 2 plitude histogram distributions for digital coherent receivers

Hao, Ming; Jiang, Xuedong; Xiong, Xingzhong; Giddings, Roger; He, Wei; Tang, Jianming

Photonics

Accepted/In press: 11/04/2023

Peer reviewed version

[Cyswllt i'r cyhoeddiad / Link to publication](#)

Dyfyniad o'r fersiwn a gyhoeddwyd / Citation for published version (APA):

Hao, M., Jiang, X., Xiong, X., Giddings, R., He, W., & Tang, J. (Accepted/In press). Low-complexity modulation format identification based on am- 2 plitude histogram distributions for digital coherent receivers. *Photonics*.

Hawliau Cyffredinol / General rights

Copyright and moral rights for the publications made accessible in the public portal are retained by the authors and/or other copyright owners and it is a condition of accessing publications that users recognise and abide by the legal requirements associated with these rights.

- Users may download and print one copy of any publication from the public portal for the purpose of private study or research.
- You may not further distribute the material or use it for any profit-making activity or commercial gain
- You may freely distribute the URL identifying the publication in the public portal ?

Take down policy

If you believe that this document breaches copyright please contact us providing details, and we will remove access to the work immediately and investigate your claim.

Low-complexity modulation format identification based on amplitude histogram distributions for digital coherent receivers

Ming Hao,^{1,2,3,4} Xuedong Jiang,¹ Xingzhong Xiong,^{1,2} Roger Giddings,³ Wei He,¹ and Jianming Tang^{3,*}

¹ School of Automation and Information Engineering, Sichuan University of Science and Engineering, Yibin 644000, China

² Artificial Intelligence Key Laboratory of Sichuan Province, Sichuan University of Science and Engineering, Yibin 644000, China

³ The DSP Centre of Excellence, School of Computer Science and Electronic Engineering, Bangor University, Bangor LL57 1UT, UK

⁴ Key Laboratory of Higher Education of Sichuan Province for Enterprise Informationalization and Internet of Things, Sichuan University of Science and Engineering, Yibin 644000, China

* Correspondence: j.tang@bangor.ac.uk

Citation: Hao, M.; Tang, J. Low-complexity modulation format identification based on amplitude histogram distributions for digital coherent receivers. *Photonics* **2023**, *10*, x. <https://doi.org/10.3390/xxxxx>

Received: date

Revised: date

Accepted: date

Published: date



Copyright: © 2023 by the authors. Submitted for possible open access publication under the terms and conditions of the Creative Commons Attribution (CC BY) license (<https://creativecommons.org/licenses/by/4.0/>).

Abstract: A prior-training-free and low-complexity modulation format identification (MFI) scheme based on amplitude histogram distributions is proposed and demonstrated, both numerically and experimentally, for autonomous digital coherent receivers. In the proposed scheme, after having performed power normalization, incoming polarization division multiplexed (PDM) signals are classified into QPSK, 8QAM, 16QAM, 32QAM and 64QAM signals according to their ratios defined according to specific features of their amplitude histograms. The proposed MFI scheme uses amplitude information only, thus it is insensitive to carrier phase noise. Furthermore, the proposed scheme does not require any prior information such as optical signal-to-noise ratio (OSNR). The performance of the proposed MFI scheme is numerically verified using 28GBaud PDM-QPSK/-8QAM/-16QAM/-32QAM/-64QAM signals. The numerical simulation results show that the proposed scheme can achieve 100% of correct identification rate for all of the five modulation formats when their OSNR values are higher than the thresholds corresponding to the 20% FEC correcting bit error rate (BER) of 2.4×10^{-2} . To further explore the effectiveness of the proposed MFI scheme, proof-of-concept experiments in 28GBaud PDM-QPSK/-8QAM/-16QAM, and 21.5GBaud PDM-32QAM transmission systems are also undertaken, which show that the proposed scheme is robust against fiber nonlinearities. To explore the scheme's feasibility for use in practical transmission systems, the computational complexity analysis of the proposed scheme is conducted, which shows that, compared with relevant MFI scheme, the proposed MFI scheme can significantly reduce the computational complexity.

Keywords: Modulation format identification, coherent optical communications, amplitude histogram distributions

1. Introduction

To meet the growing demand for supporting a wide diversity of data services such as the Internet of Things, big data, cloud computing and video streaming, spectrum-sliced elastic optical networks (EONs) [1] have been proposed, which have attracted considerable interest from the telecommunications R&D community world-wide [2], with the key focus of addressing the optical network's developing trend of evolving from fixed network architectures to future flexible and elastic ones [3, 4]. According to different transmission link conditions and various quality of service requirements, the transceivers involved in the EONs have to be capable of dynamically adjusting their operation parameters including, for example, modulation formats, symbol rates and transmission power, in order to maximize their signal transmission capacities and spectral/power utilization efficiency. In traditional optical networks, these parameters are delivered to the corresponding receivers by the supervisory control layer of the optical networks. However, if the supervisory channel is disrupted and/or does not respond to the dynamic traffic demands sufficiently fast, the digital coherent receivers may fail to work appropriately [5–7]. In addition, both the cross-layer communications and end-to-end handshaking are also regarded as the major factors limiting the flexibility of next generation optical networks. Therefore, it is highly desirable if the digital coherent receivers can autonomously identify these transmission parameters without being assisted by the supervisory control layer.

Over the aforementioned parameters, modulation format is one of the most important parameters. Real-time identifying and monitoring the modulation format for the communication scenarios with timing-varying channel characteristics where adaptive signal modulation format variations are necessary to be implemented. The use of the MFI techniques would eliminate the transmissions of signal modulation format information between the transceivers, thus considerably reducing the unwanted overhead. The MFI

algorithm can be applied before modulation format dependent algorithms including polarization demultiplexing, frequency offset compensation as well as carrier phase recovery [8], and could ensure optimal system performance.

The previously reported MFI schemes for optical fiber communications can be roughly classified into the following three categories: (1) Data-aided schemes [9–11], in which additional pilot information are introduced, and the computational complexity of the MFI scheme is thus low but with a cost of reduced spectral efficiency; (2) Schemes based on Stokes space [7, 8, 12–23]. These schemes are not sensitive to carrier phase noise, frequency offset and polarization mixing. (3) Schemes based on signal characteristics arising from constant modulus algorithm (CMA) equalization [24–33]. These schemes are based on CMA equalized signals and do not require any space mapping. Meanwhile, CMA can also compensate for residual chromatic dispersion (CD) and polarization mode dispersion (PMD). However, the major challenge for these schemes is that the modulation format features are ambiguous under the effects of noise and other transmission impairments. In recent years, due to the powerful ability of ambiguous information identification, machine learning technologies are widely employed for the identification of CMA equalized signals. These include convolutional neural network (CNN) [2], binarized neural network (BNN) [3], support vector machine (SVM) [5], random forest [6], and deep neural network (DNN) [34, 35]. Assisted by the powerful property of machine learning, these schemes are able to achieve high MFI performances. However, in order to obtain a desired optimal performance, a large number of training samples, high computational resources and a complex training process are essential for these schemes. Meanwhile, if the link conditions such as distance or another parameter changes, the machine learning models may have to be retrained [29]. Therefore, a prior-training-free and low-complexity MFI scheme is highly desirable for practical deployment.

In this paper, a prior-training-free MFI scheme based on amplitude histogram distributions is proposed for autonomous digital coherent receivers. Since there exist different amplitude levels for QPSK, 8QAM, 16QAM, 32QAM and 64QAM, the amplitude histograms of CMA equalized signals are applied to extract key features required for identifying different modulation formats. The proposed scheme mainly focus on identifying effective local features of amplitude histograms rather than global features [6, 20, 34, 36]. In the proposed MFI scheme, after having normalized the signal power, the ratios of specific parts of the amplitude histograms are calculated, based on which five modulation formats can be identified. The proposed scheme does not require any prior-training or information such as OSNR, and is also insensitive to carrier phase noise. The performance of the proposed MFI scheme is first explored by numerical simulations with 28GBaud PDM-QPSK/-8QAM/-16QAM/-32QAM/-64QAM signals. The simulation results show that the proposed scheme can achieve 100% of the correct MFI rate for all five modulation formats when the OSNR values are higher than their corresponding theoretical 20% forward error correction (FEC) limit ($\text{BER} = 2.4 \times 10^{-2}$). For 28GBaud PDM-QPSK/-8QAM/-16QAM, and 21.5GBaud PDM-32QAM systems subject to back-to-back and long-haul fiber transmission link conditions, proof-of-concept experiments are undertaken to further verify the effectiveness of the proposed MFI scheme. The experimental results show that the proposed scheme is robust against fiber nonlinearities and suitable for use in long-haul transmission links. Finally, the computational complexity of the proposed scheme is also discussed, which is considerably lower than relevant MFI scheme. The proposed scheme shows a good tradeoff between identification performance and computational complexity, and may be regarded as a good candidate for use in EONs with improved flexibility.

2. Operating principle

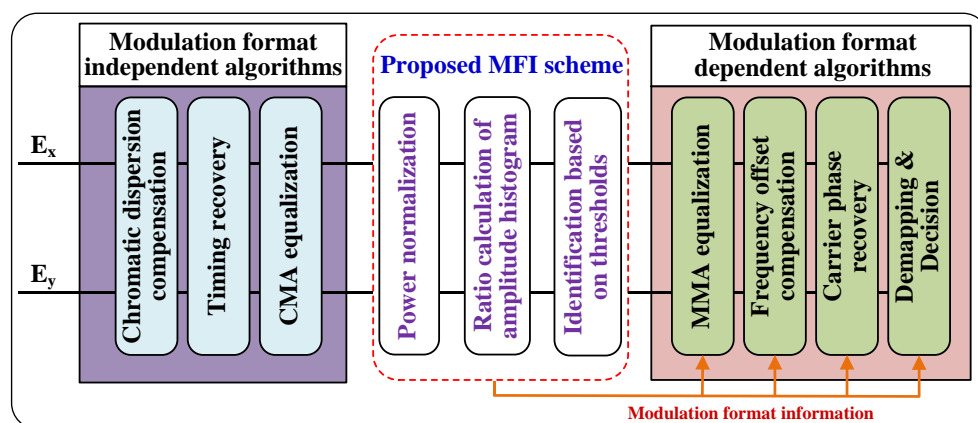


Figure 1. The DSP architecture with the proposed MFI scheme for autonomous digital coherent receivers.

The digital signal processing (DSP) procedure of the autonomous digital coherent receiver considered here is depicted in Figure 1, where the proposed MFI scheme is highlighted. Before conducting the MFI operation, modulation format-independent algorithms shown in the purple area are employed to compensate for the CD impairments and timing-jitter, and to achieve preliminary polarization demultiplexing. Here, it should be noted that m PSK signals can be completely polarization demultiplexed by CMA. Meanwhile, CMA is capable of compensating residual CD and PMD for different modulation formats [2, 5, 28, 31]. However, for m QAM ($m > 4$) signals, further polarization demultiplexing algorithm may also be required. After having performed the modulation format independent operations, the proposed MFI scheme can then be applied, whose outputs are provided to the subsequent modulation format dependent algorithms shown in the pink box, which consists of the multi-modulus algorithm (MMA), frequency offset compensation and carrier phase recovery to compensate for various transmission impairments experienced by the signals.

As illustrated in Figure 1, the proposed MFI scheme consists of three steps: first, the CMA equalized signals are power normalized. Then the amplitude histograms of the signals are obtained, and the calculations of the ratios defined below are subsequently undertaken. It should be noted that only CMA equalized signals of one polarization are required to acquire the amplitude histogram. Finally, based on the thresholds of the ratios H_1 , H_2 , H_3 and H_4 , five commonly adopted modulation formats including PDM-QPSK/-8QAM/-16QAM/-32QAM/-64QAM are identified.

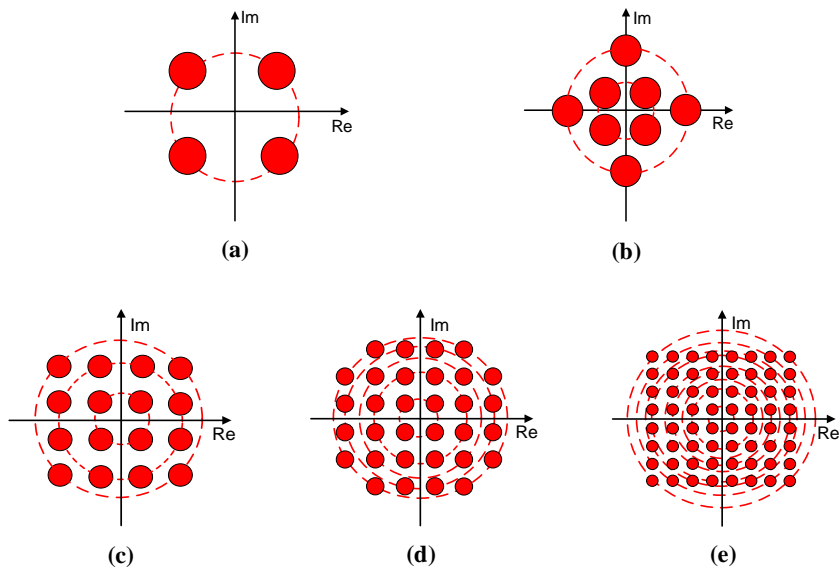


Figure 2. Constellation diagrams of five widely employed modulation formats: (a) QPSK, (b) 8QAM, (c) 16QAM, (d) 32QAM, (e) 64QAM. There are one, two, three, five, and nine amplitude levels for QPSK, 8QAM, 16QAM, 32QAM, and 64QAM, respectively.

Table 1. Amplitude value and associated probability for each level of the five modulation formats.

QPSK	Amplitude value	1								
	Associated probability	100%								
8QAM	Amplitude value	0.577			1.291					
	Associated probability	50%			50%					
16QAM	Amplitude value	0.447		1			1.342			
	Associated probability	25%		50%			25%			
32QAM	Amplitude value	0.316		0.707		0.949		1.14		1.304
	Associated probability	12.5%		25%		12.5%		25%		25%
64QAM	Amplitude value	0.218	0.488	0.655	0.787	0.9	1.091	1.175	1.327	1.528
	Associated probability	6.25%	12.5%	6.25%	12.5%	12.5%	18.75%	12.5%	12.5%	6.25%

As shown in Figure 2, there are one, two, three, five, and nine amplitude levels for QPSK, 8QAM, 16QAM, 32QAM, and 64QAM, respectively. For each level of these five modulation formats, the amplitude value and its associated probability are presented in Table 1. Without loss of generality, the symbols of each modulation format are assumed to have a unit average power [37]:

$$\sum_{n=1}^m p_n \cdot Z_n^2 = 1 \quad (1)$$

where Z_n is the amplitude value and p_n is the associated probability for the n -th level, and m is the number of total levels for the considered modulation format. The amplitude levels of the different modulation formats can be clearly seen in Figure 2. However, in practical transmission systems, the distributions of the amplitude levels may be indistinct even if CD, timing-jitter, and part of polarization mixing are compensated by the modulation format independent algorithms, thus it is difficult to identify high-order modulation formats, especially for low OSNR cases. To address such a challenge, the amplitude histogram of the CMA equalized signals is employed to identify these five modulation formats over a considerably widened OSNR range.

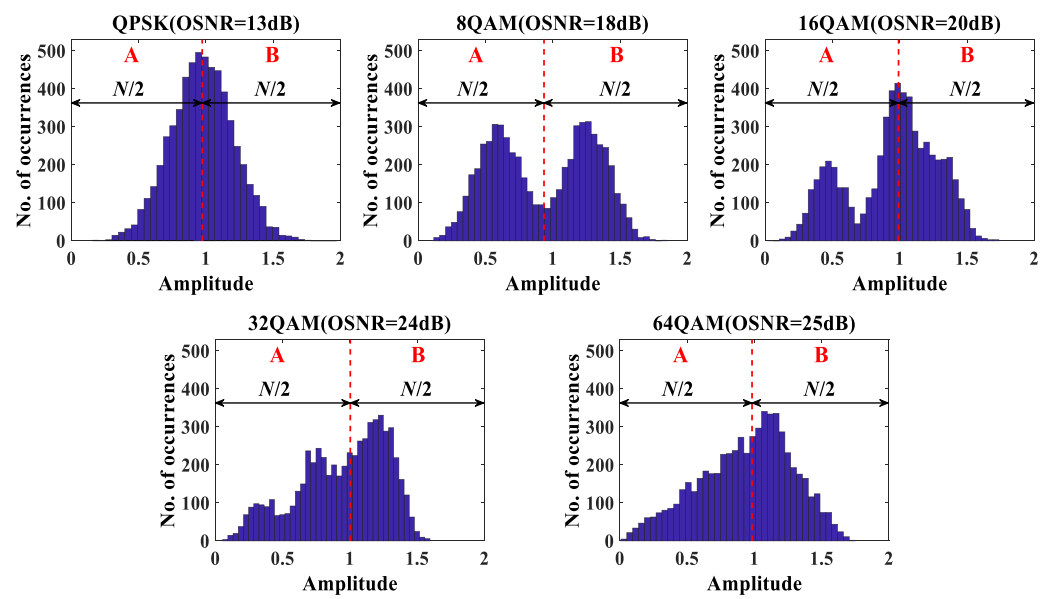


Figure 3. The first partition operation for the amplitude histograms of QPSK, 8QAM, 16QAM, 32QAM and 64QAM. The amplitude histograms are divided into two parts based on the number of symbols, which is $N/2$ in both part A and B.

The amplitude histograms of these five modulation formats are shown in Figure 3, where the OSNR values for the PDM-QPSK/-8QAM/-16QAM/-32QAM/-64QAM signals are fixed at 13dB, 18dB, 20dB, 24dB and 25dB, respectively. For all of the amplitude histograms illustrated in Figure 3, the total number of symbols N is 6000, the same N value is also utilized in Figures 4 and 5, and the bin number of all of the amplitude histograms is 40. The first partition operation is employed for the sake of separation between 8QAM and other four modulation formats. The amplitude histograms are divided into two parts based on the number of symbols, which is $N/2$ in both part A and B. Since 8QAM includes two amplitude levels, as mentioned in Table 1, the signal amplitudes for part A concentrate around 0.577 while for part B the amplitudes concentrate around 1.291 even in the presence of noise. In other words, the average signal amplitude for part B is about doubled compared to part A. The corresponding ratio for the 8QAM signals is the largest among the five modulation formats. In this case, the ratio H_1 is defined as

$$H_1 = \frac{H_{B1}}{H_{A1}} \quad (2)$$

$$\text{where: } H_{A1} = m_1 \times c_1 + \dots + m_i \times c_i + \left(\frac{N}{2} - \sum_{x=1}^i m_x\right) \times c_{i+1}, \quad \sum_{x=1}^i m_x \leq \frac{N}{2}, \quad \sum_{x=1}^{i+1} m_x > \frac{N}{2}. \quad m_i \text{ de-} \quad 172$$

$$H_{B1} = \left(\sum_{x=1}^{i+1} m_x - \frac{N}{2}\right) \times c_{i+1} + m_{i+2} \times c_{i+2} + \dots + m_{nbins} \times c_{nbins} \quad 173$$

notes the number of symbols in the i -th bin, c_i represents the central amplitude value of the i -th bin, N indicates the total number of symbols, and $nbins$ is the total number of bins. In order to accurately divide the amplitude histogram into two parts, the symbols in $i+1$ bin is divided into two different parts, $\frac{N}{2} - \sum_{x=1}^i m_x$ symbols are divided into part A, while

$$\sum_{x=1}^{i+1} m_x - \frac{N}{2} \text{ symbols are divided into part B.} \quad 177$$

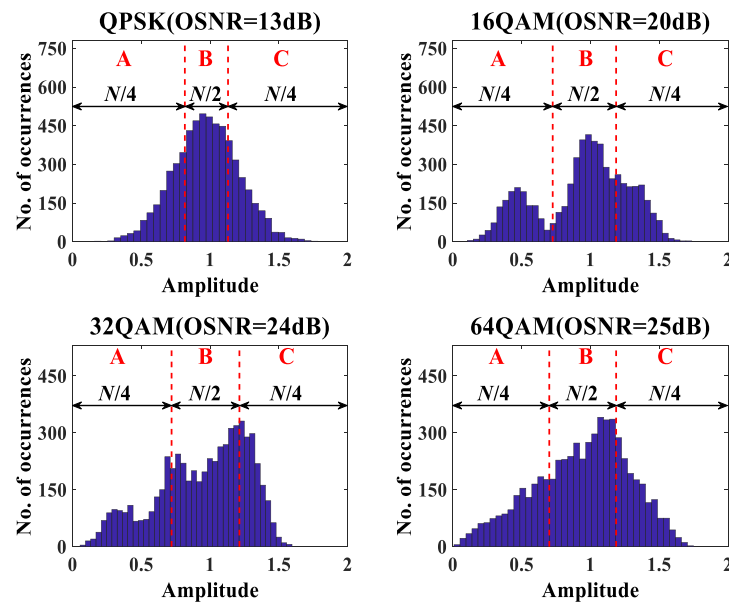


Figure 4. The second partition operation for the amplitude histograms of QPSK, 16QAM, 32QAM and 64QAM. The amplitude histograms of the four modulation formats are divided into part A, B and C. The number of symbols in part A, B and C are $N/4$, $N/2$ and $N/4$, respectively.

Since 8QAM can be distinguished based on the ratio H_1 , the purpose of the second partition operation is to identify QPSK from other three modulation formats. As shown in Figure 4, the amplitude histograms of the remaining four modulation formats are divided into part A, B and C. The number of symbols in part A, B and C are $N/4$, $N/2$ and $N/4$, respectively. Due to the constant amplitude, the distribution of amplitudes for QPSK still concentrate around 1 even in the presence of noise. As a result, compared with the three other modulation formats, the amplitude distribution of the QPSK signals in part A and C is much closer. However, because of the influence of noise, such a distribution feature gradually becomes less obvious for low OSNR cases. To address this problem, a square operation of the number of symbols in each individual bin is conducted, and the corresponding ratio H_2 is defined as

$$H_2 = \frac{H_{C2}}{H_{A2}} \quad (3) \quad 193$$

$$\text{where: } H_{A2} = m_1^2 \times c_1 + \dots + m_i^2 \times c_i + \left(\frac{N}{4} - \sum_{x=1}^i m_x\right)^2 \times c_{i+1}, \quad \sum_{x=1}^i m_x \leq \frac{N}{4}, \quad \sum_{x=1}^{i+1} m_x > \frac{N}{4} \quad 194$$

$$H_{C2} = \left(\sum_{x=1}^{j+1} m_x - \frac{3N}{4}\right)^2 \times c_{j+1} + m_{j+2}^2 \times c_{j+2} + \dots + m_{nbins}^2 \times c_{nbins}, \quad \sum_{x=1}^j m_x \leq \frac{3N}{4}, \quad \sum_{x=1}^{j+1} m_x > \frac{3N}{4} \quad 194$$

Since the closer amplitude distributions of part A and C, the ratio H_2 for QPSK is smaller than that of the three remaining modulation formats, thus QPSK can be identified. After that, the partition of the amplitude histogram remains unchanged. The difference is that only part B and C are taken into consideration. The ratio H_3 is introduced and can be calculated as

$$H_3 = \frac{H_{B3}}{H_{C3}} \quad (4)$$

$$\text{where: } H_{B3} = \left(\sum_{x=1}^{i+1} m_x - \frac{N}{4} \right)^2 \times c_{i+1} + m_{i+2}^2 \times c_{i+2} + \dots + \left(\frac{3N}{4} - \sum_{x=1}^j m_x \right)^2 \times c_{j+1}, \quad \sum_{x=1}^i m_x \leq \frac{N}{4},$$

$$\sum_{x=1}^{i+1} m_x > \frac{N}{4}, \quad \sum_{x=1}^j m_x \leq \frac{3N}{4}, \quad \sum_{x=1}^{j+1} m_x > \frac{3N}{4}, \quad H_{C3} = H_{C2}.$$

Due to the square operation of the number of symbols in each bin, the distributions in part B and/or part C are more concentrated, thus the values of H_{B3} and/or H_{C3} are greater. It can be clearly seen in Table 1 that, for 32QAM, all of the symbols in part C concentrate around the fifth amplitude level while the symbols in part B spread over three different amplitude levels. Thus, the ratio H_3 for 32QAM is small. Unlike 32QAM, the symbols for 64QAM in part C spread over three different amplitude levels. H_{C3} of 64QAM is thus much smaller than that of 32QAM. For 16QAM, the symbols in part B and part C are concentrated around the second and third amplitude levels, respectively. H_{B3} of 16QAM is much greater than that of 32QAM. Without considering noise and/or any other transmission impairments, the theoretical value of H_3 for 16QAM, 32QAM and 64QAM are 2.98, 1.19 and 2.21, respectively. Nevertheless, as the effect of noise is increased for the low OSNR cases, the symbols of 32QAM in part C is dispersed, which results in an increased value of H_3 . Incorrect decisions may be made between H_3 of 16QAM for high OSNR cases and H_3 of 32QAM for low OSNR cases. Therefore, only relying solely on a single ratio H_3 cannot accurately distinguish 32QAM from 16QAM over a wide OSNR range. To address this problem, an additional ratio is also required, as detailed below.

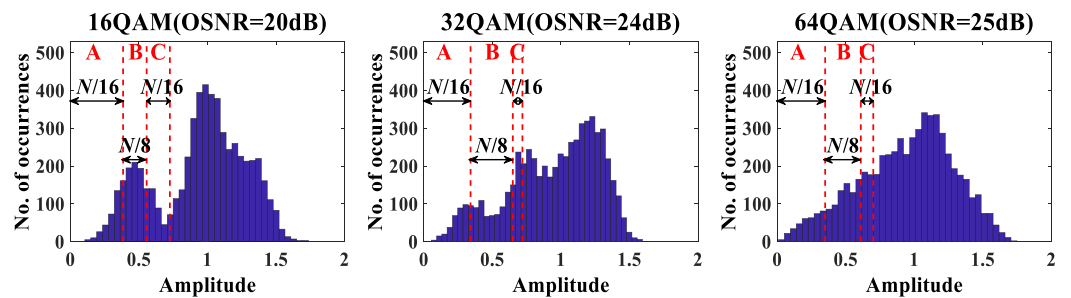


Figure 5. The third partition for the amplitude histograms of 16QAM, 32QAM and 64QAM. The first $N/4$ symbols are divided into three parts. The number of symbols in part A, B and C are $N/16$, $N/8$ and $N/16$, respectively.

As seen in Figure 5, the third partition of the amplitude histogram is to divide the first $N/4$ symbols into three parts. The number of symbols in part A, B and C are $N/16$, $N/8$ and $N/16$, respectively. As listed in Table 1, the first $N/4$ symbols in the amplitude histogram correspond to only one amplitude value for 16QAM, while the symbols for 32QAM and 64QAM correspond to two and three amplitude values, respectively. Even under the effect of noise, for 16QAM, the distribution of amplitudes in part A and C still concentrate around 0.447. By comparison, the distributions of part A and C spread more widely for 32QAM and 64QAM. Therefore, the ratio H_4 is introduced and defined as

$$H_4 = \frac{H_{C4}}{H_{A4}} \quad (5)$$

where:

$$H_{A4} = m_1 \times c_1 + \dots + m_i \times c_i + \left(\frac{N}{16} - \sum_{x=1}^i m_x\right) \times c_{i+1}$$

$$H_{C4} = \left(\sum_{x=1}^{j+1} m_x - \frac{3N}{16}\right) \times c_{j+1} + m_{j+2} \times c_{j+2} + \dots + \left(\frac{N}{4} - \sum_{x=1}^k m_x\right) \times c_{k+1}$$

$$\sum_{x=1}^i m_x \leq \frac{N}{16}, \quad \sum_{x=1}^{i+1} m_x > \frac{N}{16}$$

$$\sum_{x=1}^j m_x \leq \frac{3N}{16}, \quad \sum_{x=1}^{j+1} m_x > \frac{3N}{16}, \quad \sum_{x=1}^k m_x \leq \frac{N}{4}, \quad \sum_{x=1}^{k+1} m_x > \frac{N}{4}$$

Due to the more concentrated distribution, H_{A4} of 16QAM is relatively larger than those related to 32QAM and 64QAM, while H_{C4} is relatively smaller than those related to 32QAM and 64QAM, which results in a smaller H_4 . As a direct result, 16QAM and 32QAM can be identified over a wide OSNR range by making use of both H_3 and H_4 . Meanwhile, although 16QAM and 64QAM can be distinguished by relying on H_4 only, as seen in Figure 6, the utilization of both H_3 and H_4 is necessary for identifying 16QAM.

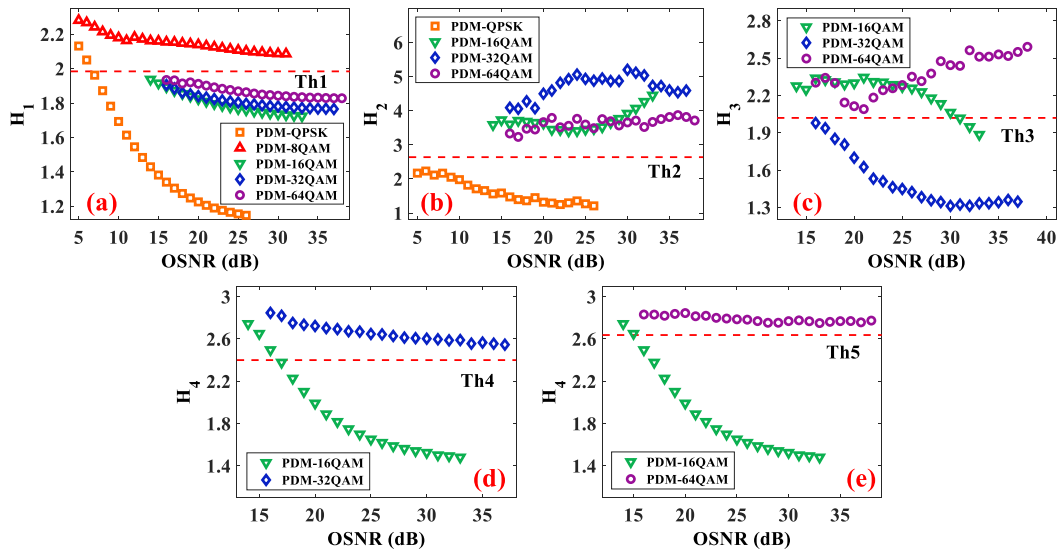


Figure 6. H_1 , H_2 , H_3 and H_4 vary with the OSNR in the back-to-back simulation. The dotted red lines indicate the corresponding thresholds.

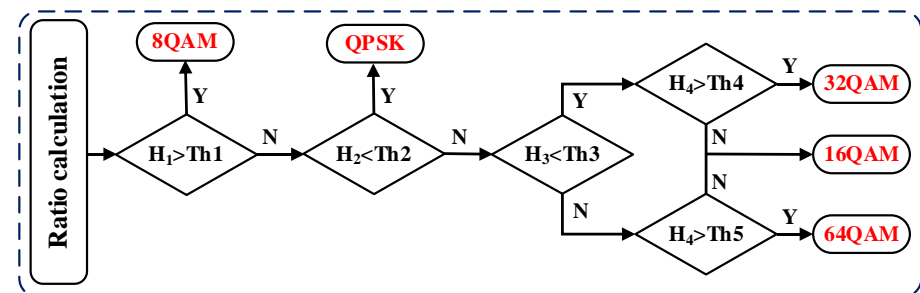


Figure 7. Flow chart of the proposed MFI scheme.

As already mentioned above, the different modulation formats give rise to different ratios. Figure 6 shows the values of H_1 , H_2 , H_3 and H_4 for the five modulation formats in different OSNR cases. The number of symbols is 6000, and the bin number of the amplitude histogram is 40. By selecting appropriate thresholds, the incoming PDM signals can

be identified as QPSK, or 8QAM, or 16QAM, or 32QAM or 64QAM signals. The corresponding thresholds of H_1 , H_2 , H_3 and H_4 are 1.984, 2.64, 2.02 and 2.4/2.637, respectively, as indicated by the dotted red lines in Figure 6. It should be noted that there are two thresholds of H_4 for distinguishing 16QAM from 32QAM (2.4) and 64QAM (2.637). The thresholds for H_1 , H_2 , H_3 and H_4 are determined to balance the optimal identification performance of each identified modulation format. Figure 7 illustrates a flow chart of the proposed MFI scheme. If H_1 of the incoming signals is greater than 1.984, the signals can be recognized as 8QAM signals, otherwise, if H_2 of the incoming signals is less than 2.64, the signals can be identified as QPSK signals. The remaining 16QAM, 32QAM and 64QAM can be further distinguished by making use of both H_3 and H_4 .

3. Numerical simulation results

VPI Transmission Maker 9.8 is utilized to undertake a series of numerical simulations to extensively verify the proposed MFI scheme. The length of pseudo-random bit sequence (PRBS) is $2^{15}-1$. 28GBaud PDM-QPSK/-8QAM/-16QAM/-32QAM/-64QAM signals are generated in the transmitter. The sample rate is 56GSa/s, and the roll-off factor of the square root raised cosine (SRRC) filter is 0.1. The wavelength and linewidth of the laser are 1550nm and 100kHz, respectively. The modulated signals are then passed through an additive Gaussian white noise (AWGN) channel with adjustable OSNRs calculated at a 0.1nm ASE noise bandwidth. These PDM signals are finally detected and their modulation formats are identified by a coherent receiver utilizing an off-line DSP module based on the proposed MFI scheme, as shown in Figure 1. The OSNR ranges of the PDM-QPSK/-8QAM/-16QAM/-32QAM/-64QAM signals are 5-26dB, 5-31dB, 14-33dB, 16-37dB and 16-38dB, respectively, with an OSNR incremental of 1dB. In order to evaluate the performance of the proposed scheme, for each modulation format, 100 independent simulations are conducted for each OSNR value.

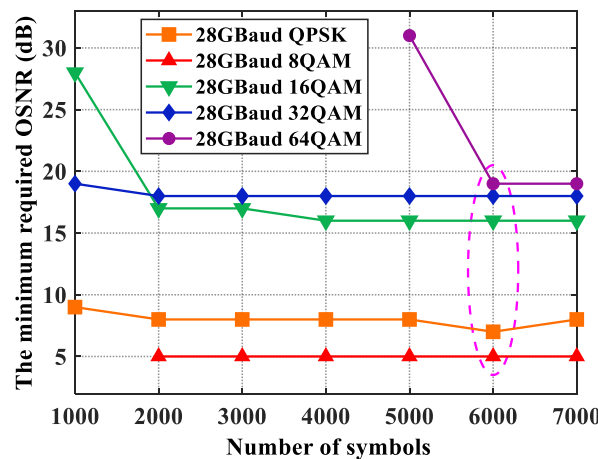


Figure 8. Minimum required OSNR values with different number of symbols for five modulation formats. 6000 symbols is optimum selection.

For a MFI scheme, the minimum required number of symbols, which corresponds to the lowest OSNR required for the considered modulation format, is one of the most important factors, because it determines the response-speed and computational complexity of the MFI algorithm [28, 32]. The minimum required OSNR values versus number of symbols for the five modulation formats are shown in Figure 8, where the symbol variation range varies from 1000 to 7000 at an interval of 1000. For QPSK, 8QAM, 16QAM and 32QAM, when the number of symbols is greater than or equal to 2000, the minimum required OSNR value to achieve a correct identification rate of 100% remains almost constant. Whilst since 64QAM is the highest order of modulation format with more amplitude levels, an efficient feature extraction requires more symbols to be employed. If the number

of symbols is lower than 6000, the minimum required OSNR value increases substantially. Since the required number of symbols for the proposed MFI scheme is determined by the highest order modulation format, thus the numbers of symbols for all of the considered modulation formats are set at 6000 in the following numerical simulations and proof-of-concept experiments. It should be noted that when the number of symbols is lower than 2000 or 5000 for 8QAM or 64QAM respectively, a correct identification rate of 100% cannot be obtained.

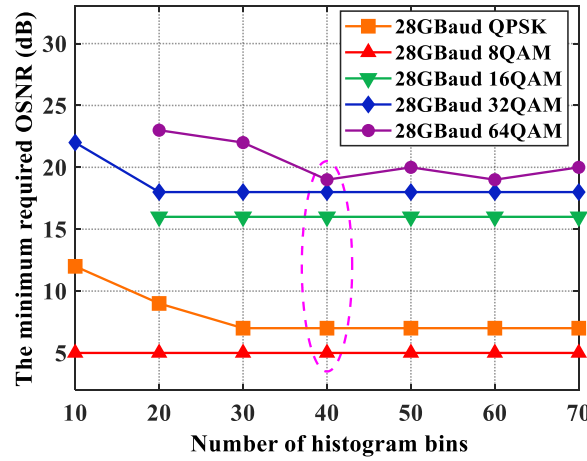


Figure 9. Minimum required OSNR values with different number of histogram bins for five modulation formats. 40 bins is optimum selection.

The number of histogram bins is another factor that also determines the computational complexity of the proposed MFI scheme. Similar to the number of symbols, an optimal number of the histogram bin is also identified as it gives rise to the minimum required OSNR value, as shown in Figure 9. If the number of histogram bins is less than 40, the minimum required OSNR values increases gradually especially for 64QAM. As a result, in order to achieve an optimum tradeoff between computational complexity and MFI performance, the number of histogram bins for the five modulation formats are taken to be 40 in the following numerical simulations and proof-of-concept experiments.

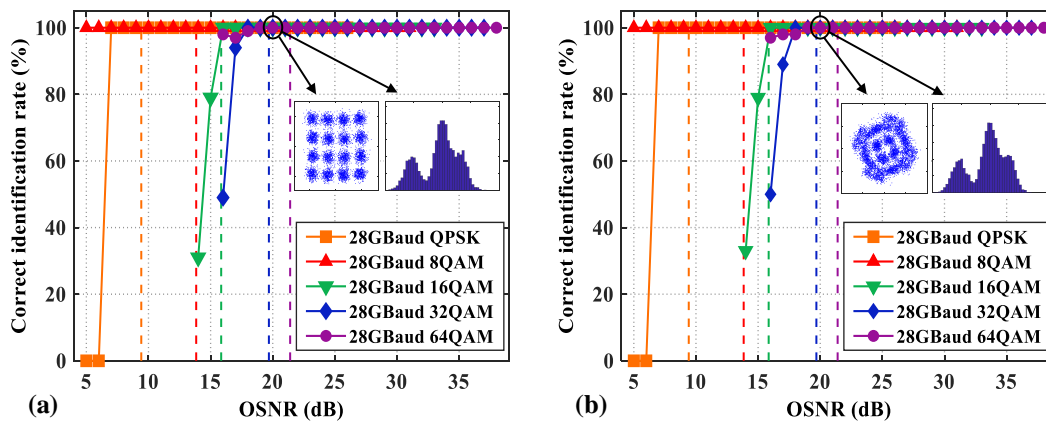


Figure 10. Simulation results of correct identification rate versus OSNR value under different linewidth: (a) 0Hz; (b) 100kHz. The illustrations are the constellation diagrams and amplitude histograms of PDM-16QAM when the linewidth is 0Hz or 100kHz, respectively. The vertical dash lines indicate the OSNR thresholds corresponding to the 20% FEC correcting BER of 2.4×10^{-2} .

In order to analyze the influence of carrier phase noise on the performance of the proposed MFI scheme, the simulation results of correct identification rate versus OSNR

value under different linewidth are shown in Figure 10(a) and (b), respectively. Compared with Figure 10(a), when the linewidth of the laser is 100kHz, the constellation of 16QAM rotates, as shown in Figure 10(b), due to the existence of carrier phase noise. However, since the amplitude histogram depends on amplitude information only, the effect of carrier phase noise on amplitude histogram is almost negligible. Therefore, as shown in Figure 10(a) and (b), when the value of linewidth is increased from 0Hz to 100kHz, the minimum required OSNR values to achieve a correct identification rate of 100% for the five modulation formats remains unchanged. In conclusion, the proposed MFI scheme is insensitive to carrier phase noise.

To explore the OSNR-dependent correct identification rate performance of the proposed MFI scheme under typical value of linewidth, for different signal modulation formats, their numerically simulated correct identification rates as a function of OSNR are shown in Figure 10(b). The simulation results show that 100% accurate identification can be obtained for 8QAM even when the OSNR values are very low (5dB). For QPSK, 16QAM, 32QAM and 64QAM, the minimum OSNR values for achieving the correct identification rate of 100% are 7dB, 16dB, 18dB and 19dB, respectively. As seen in Figure 10(b), the proposed MFI scheme can achieve a correct identification rate of 100% for all of the five modulation formats when the OSNR values are higher than their thresholds (indicated by vertical dash lines) corresponding to the 20% FEC correcting BER of 2.4×10^{-2} .

By making use of the incoming signals identical to those presented above, the performance of the proposed scheme is further evaluated in comparison with schemes using DNN, SVM, modified particle swarm optimization (M-PSO) [20] and principal component analysis of Stokes parameters (PCASP) [8]. The SVM and DNN schemes also adopt the amplitude histogram as the proposed scheme. The number of symbols and histogram bins are fixed at 6000 and 40, respectively. To ensure the optimal performance, a large training data set for DNN is required. Such training set comprises 9200 ($18 \times 100 + 23 \times 100 + 15 \times 100 + 17 \times 100 + 19 \times 100$) amplitude histograms. In this work, a four-layer DNN is employed, in which the number of neurons in the input, first hidden, second hidden and output layer are 40, 40, 10 and 5, respectively. The activation functions of the hidden layer and output layer are *ReLU* and *softmax*, respectively [6]. On the other hand, since the complexity of SVM is related to the number of support vectors, by considering the tradeoff between the identification performance and the computational complexity for SVM, the training set of SVM comprises 3640 ($18 \times 40 + 23 \times 40 + 15 \times 40 + 17 \times 40 + 18 \times 40$) amplitude histograms. For SVM, the kernel function is the default radial basis function (RBF) kernel [38].

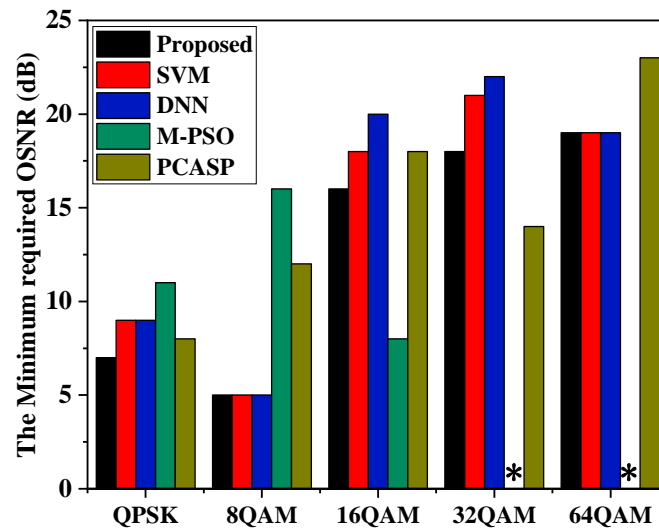


Figure 11. Minimum required OSNR for identifying different modulation formats for five MFI schemes.

The minimum required OSNR comparisons between the proposed scheme and these four schemes are shown in Figure 11. * indicates the modulation format is not identified by this scheme. Scheme based on M-PSO can only identify three modulation formats including QPSK, 8QAM and 16QAM, and the minimum required OSNR for identifying QPSK and 8QAM is much higher than that of the proposed scheme. The minimum required OSNRs of the proposed scheme to identify each modulation format are both lower than that of Scheme based on PCASP except 32QAM. For QPSK, 16QAM and 32QAM, the minimum required OSNR values for the proposed scheme are lower than those corresponding to DNN and SVM. For 8QAM and 64QAM, the proposed scheme offers minimum required OSNRs identical to DNN and SVM. The reason why the proposed scheme can improve the performances is that the proposed scheme mainly focus on identifying effective local features, while the MFI ability of DNN and SVM at a cost of higher complexity focus on identifying global features. Furthermore, DNN and SVM also require more details of amplitude histogram to complete the automatic feature extraction, thus 6000 symbols and 40 bins are not sufficient, this gives rise to slower response-speeds and increased computational complexity, as mentioned above.

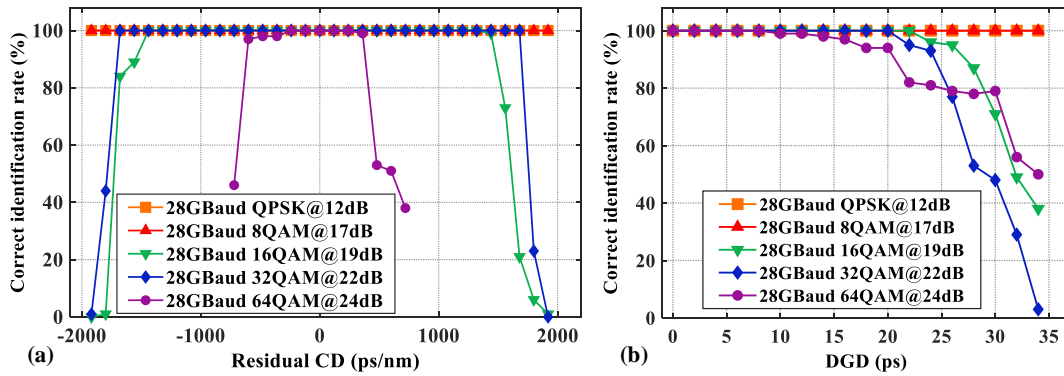


Figure 12. The tolerance with respect to (a) residual CD and (b) DGD of the proposed scheme.

In order to evaluate the effects of residual CD and PMD on the identification performance of the proposed MFI scheme, numerical simulation has been employed. It should be noted that, as shown in Fig. 1, the proposed MFI scheme is placed after CMA equalization. The CMA could compensate residual CD and PMD. Therefore, the tolerance with respect to residual CD and PMD of proposed scheme embedded in such DSP architecture is enhanced. The tolerance with respect to residual CD and DGD of the proposed scheme is shown in Figure 12 (a) and (b), respectively. The OSNR values of PDM-QPSK/-8QAM/-16QAM/-32QAM/-64QAM are 12dB, 17dB, 19dB, 22dB and 24dB, respectively. The range of residual CD for PDM-QPSK/-8QAM/-16QAM/-32QAM signals is from -1920ps/nm to 1920ps/nm, while the range of residual CD for PDM-64QAM is -720ps/nm~720ps/nm. The step for all modulation formats are both 120ps/nm. As shown in Figure 12 (a), the proposed MFI scheme can tolerate a relatively wide range of residual CD for PDM-QPSK (-1920ps/nm~1920ps/nm), PDM-8QAM (-1920ps/nm~1920ps/nm), PDM-16QAM (-1440ps/nm~1320ps/nm) and PDM-32QAM (-1680ps/nm~1680ps/nm) signals. Because of the more amplitude levels, for PDM-64QAM, the proposed scheme can tolerate residual CD from -240ps/nm to 240ps/nm.

The range of DGD for PDM-QPSK/-8QAM/-16QAM/-32QAM/-64QAM signals is from 0ps to 34ps with a step size of 2ps. Analogous to residual CD, the tolerable DGD for PDM-64QAM is much lower than other four modulation formats. The proposed scheme could achieve 100% of correct identification rate for PDM-64QAM when the DGD are 8ps.

For PDM-16QAM and PDM-32QAM, the tolerable DGDs are 22 and 20ps, respectively. The correct identification rate of PDM-QPSK and PDM-8QAM remains 100% over the whole DGD range.

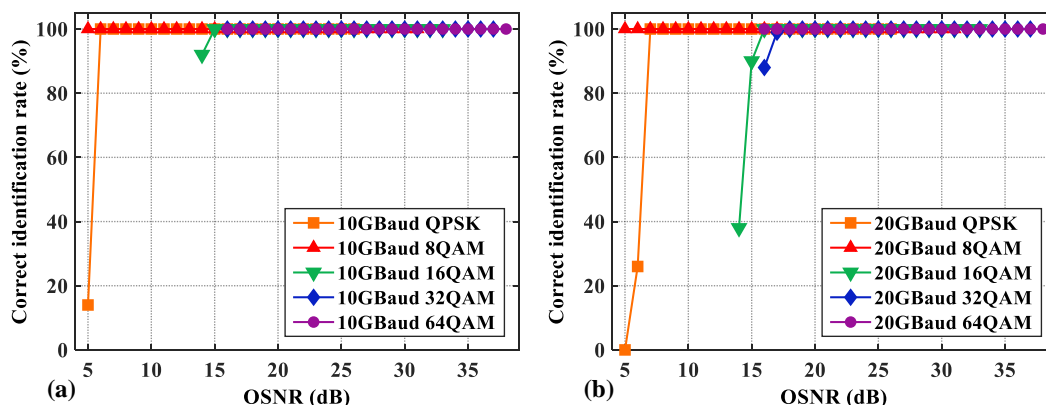


Figure 13. Simulation results of correct identification rate versus OSNR value under different baud rate: (a) 10GBaud; (b) 20GBaud.

In order to analyze the relationship between MFI performance and baud rate, *VPI Transmission Maker 9.8* is utilized to undertake numerical simulations for 10GBaud and 20GBaud transmission systems. The numerical simulation setup remains unchanged except for baud rates. Simulated correct identification rates for the five modulation formats used in the 10GBaud and 20GBaud systems are shown in Figure 13(a) and (b), respectively. These figures show that compared with the 28GBaud case shown in Figure 10(b), the MFI performances are relatively better because the tolerance to noise is improved for the lower baud rate cases.

To discuss the scalability of the proposed scheme, the MFI performance for probabilistic shaping (PS) QAM signals is also investigated. The amplitude value and its associated probability for each level of the PS-QAM signals including PS-16QAM (3bit/symbol) and PS-64QAM (5bit/symbol) are shown in Table 2. Since the probability distribution feature of the PS-QAM signals is different from that of the traditional QAM signals, the procedure and corresponding thresholds of the proposed scheme need to be modified accordingly, as detailed below.

Table 2. Amplitude value and associated probability for each level of PS-16QAM and PS-64QAM signals.

PS-16QAM(3bit/symbol)	Amplitude value	0.731			1.634			2.193		
	Probability	79.4%			19.4%			1.2%		
PS-64QAM(5bit/symbol)	Amplitude value	0.363	0.812	1.090	1.310	1.498	1.817	1.957	2.210	2.543
	Probability	28.7%	34.68%	10.38%	12.5%	7.35%	4.11%	1.65%	0.58%	0.05%

The numerical simulation setup remains unchanged except for the process used in generating the PS-16QAM and PS-64QAM signals. After power normalization, the first partition operation for the amplitude histograms of QPSK, 8QAM, PS-16QAM, 32QAM and PS-64QAM are employed. As shown in Figure 14(a), the number of symbols is $N/2$ in both part A and part B. Since part A of PS-64QAM concentrates around low amplitude

values (the associated probability for 0.363 is 28.7%), and the amplitude distribution range of part B is wide, as shown in Figure 14(c), the ratio H_1 (mentioned in Eq.(2)) of PS-64QAM is greater than that of 8QAM over a wide OSNR range. Therefore, two thresholds for H_1 are set: Th1 is 2.23 and Th2 is 2.04. Based on these two thresholds of H_1 , 8QAM is not only distinguishable from QPSK, PS-16QAM and 32QAM, but also recognizable from PS-64QAM. The second partition operation for the amplitude histograms of the rest of these modulation formats (QPSK, PS-16QAM and 32QAM) is shown in Figure 14(b). The number of symbols in part A, part B and part C are $N/4$, $N/2$ and $N/4$, respectively. The distribution of PS-16QAM in part B is more concentrated than that of QPSK and 32QAM, while the distribution of PS-16QAM in part C is dispersed. Therefore, as shown in Figure 14 (d), the value of H_3 (mentioned in Eq.(4)) for PS-16QAM is greater than those for QPSK and 32QAM. QPSK can also be distinguishable from 32QAM based on another threshold of H_3 . The two thresholds of H_3 are 4.12 (Th3) and 2.3 (Th4). The correct identification rate for identifying QPSK, 8QAM, PS-16QAM, 32QAM and PS-64QAM are shown in Figure 14(e). The proposed MFI scheme can still achieve a 100% correct identification rate for all of these five modulation formats over a wide OSNR range. The scalability of the proposed scheme is verified by the simulation results. It should also be noted that if the information entropy changes, the probability distribution features of PS-QAM also change. As such when PS-QAM with different information entropy needs to be identified, corresponding modifications to the procedure of the proposed MFI scheme and their relevant thresholds must be made. The proposed scheme is suitable for application scenarios where the set of the modulation formats that needs to be identified from are made known before applying the MFI scheme.

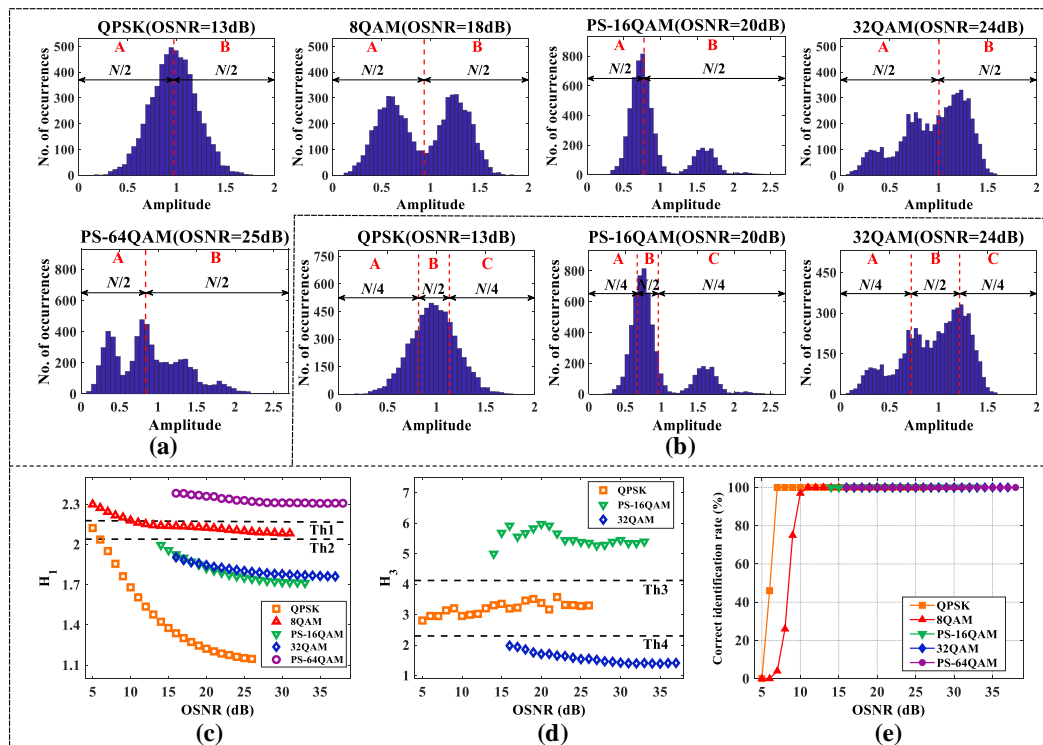


Figure 14. Operating principle and simulation results for identifying five modulation formats including PS-QAM. (a) The first partition operation and (b) second partition operation for the amplitude histograms of QPSK, 8QAM, PS-16QAM, 32QAM and PS-64QAM; (c) H_1 and (d) H_3 vary with the OSNR of the back-to-back optical transmission system, and (e) the correct identification rate for identifying these five modulation formats.

4. Experimental setup and results

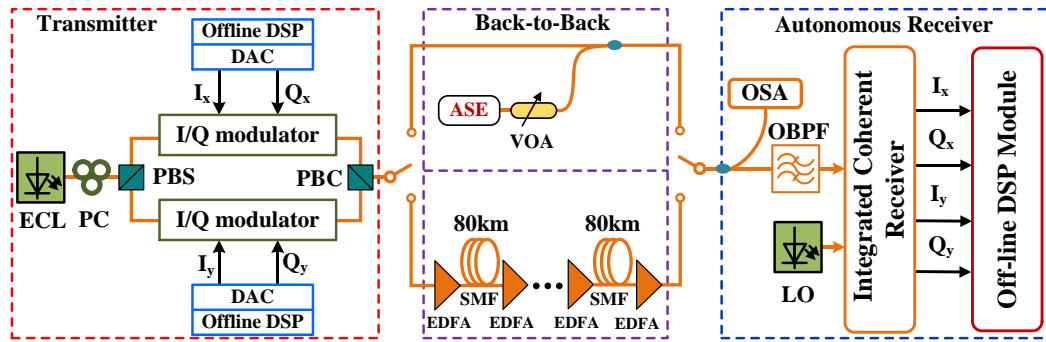


Figure 15. Proof-of-concept experimental setup of the proposed scheme. PC: polarization controller, PBS: polarization beam splitter, PBC: polarization beam coupler, VOA: variable optical attenuator, LO: local oscillator.

To experimentally verify the effectiveness of our proposed MFI scheme, a series of proof-of-concept experimental demonstrations are undertaken, whose setup is shown in Figure 15. In the transmitter, a PRBS with a word length of $2^{15}-1$ is generated by offline DSP and mapped onto different modulation formats with 2 samples/symbol. A SRRC filter with a roll-off factor of 0.1 is employed to shape the up-sampled signals. In addition, a pre-distortion operation is also applied to compensate for the frequency roll-off effect associated with the digital to analog converters (DACs). An external cavity laser (ECL) produces a continuous wave optical carrier with a wavelength of $\sim 1550\text{nm}$ and a linewidth of $\sim 100\text{ kHz}$, which is then modulated by an integrated LiNbO_3 polarization-multiplexing I/Q modulator. The DACs operating at 64GSa/s and 25GHz analog bandwidth drive four branches of the modulator to generate 28GBaud PDM-QPSK/-8QAM/-16QAM, and 21.5GBaud PDM-32QAM optical signals. The transmission links include back-to-back and long-haul fiber transmissions. The long-haul transmission link is composed of multi-spans single mode fiber (SMF) whose dispersion parameter, attenuation, and nonlinear coefficient are $D = 16.9\text{ ps/nm/km}$, $\alpha = 0.2\text{ dB/km}$, and $\gamma = 1.27\text{ km}^{-1}\cdot\text{W}^{-1}$, respectively. To completely compensate for the fiber loss, an erbium doped fiber amplifier (EDFA) with a noise figure of $\sim 5\text{dB}$ is applied in each span. An optical spectrum analyzer (OSA ANRITSU MS9740A) is used before the receiver to measure the OSNR in back-to-back case, and an optical band-pass filter (OBPF) whose bandwidth is 200GHz is employed to suppress out-of-band ASE noise. After passing through the link, the received signals are detected by an integrated coherent receiver, and then sampled by a real-time digital oscilloscope with 80GSa/s and 33GHz electrical bandwidth. Finally, these signals are processed by an off-line DSP module where the proposed MFI scheme is embedded. The frame synchronization is achieved by the auto-correlation detection of synchronization codes. The OSNR dynamic ranges for PDM-QPSK/-8QAM/-16QAM/-32QAM signals in the back-to-back links are $10\text{-}17\text{dB}$, $15\text{-}28\text{dB}$, $16\text{-}28\text{dB}$ and $18\text{-}35\text{dB}$, respectively. The step of variable OSNR is 1dB . In all of the proof-of-concept experiments, 100 samples of independent data are applied for each OSNR or launch power value.

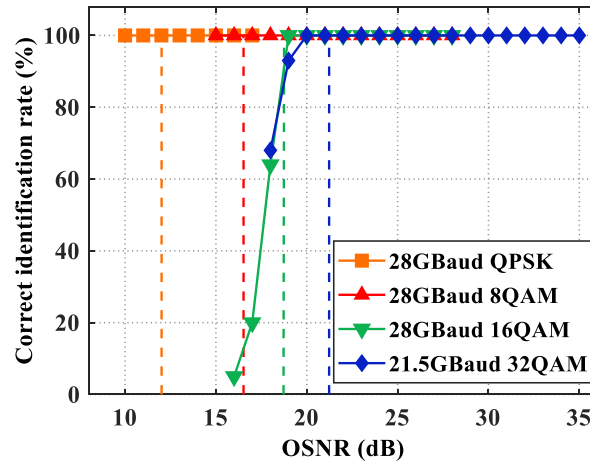
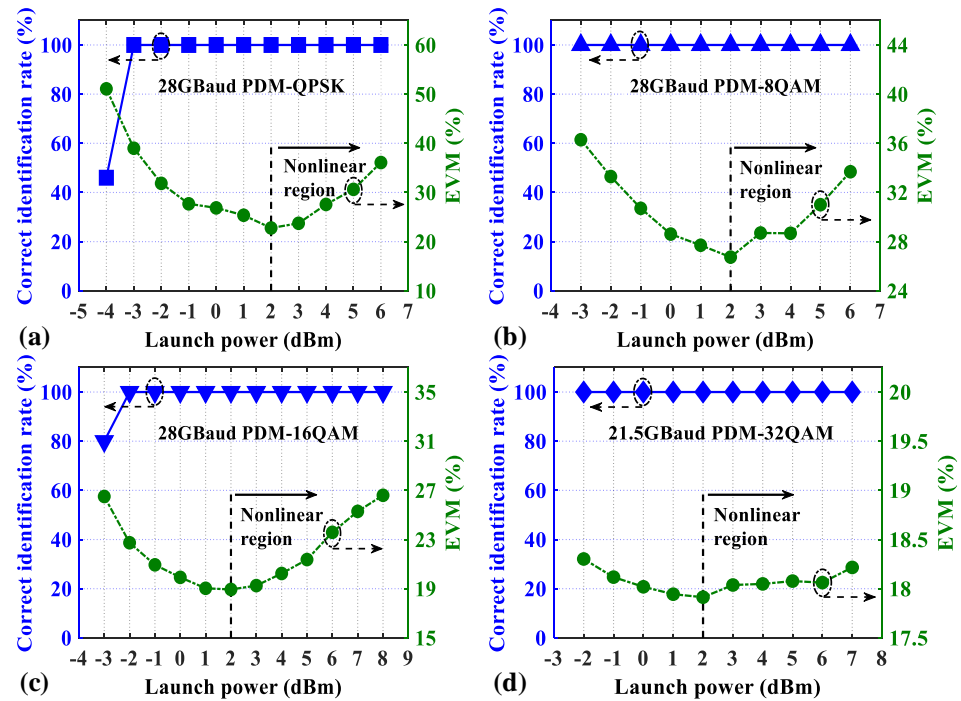


Figure 16. Correct identification rates under different OSNR values in back-to-back experiments. The vertical dash lines indicate the OSNR thresholds corresponding to 7% FEC correcting BER of 3.8×10^{-3} .

The performance of the proposed MFI scheme is first experimentally verified in back-to-back links. As shown in Figure 16, the proposed scheme achieves 100% of correct identification rate for both QPSK and 8QAM over the whole OSNR ranges considered in the experiments. The minimum OSNR values required by 16QAM and 32QAM for achieving a correct identification rate of 100% are 19dB and 20dB, respectively. Compared with the numerical simulation results, the minimum required OSNR values for these two modulation formats increase slightly. This may be due to the unwanted effects associated with the signal generation of high-order modulation formats in the experiments. The four modulation formats can still be identified with a 100% correct identification rate when their OSNR values are higher than the thresholds (indicated by the vertical dash lines) corresponding to the 7% FEC correcting BER of 3.8×10^{-3} .



478

479

480

481

482

483

484

485

486

487

488

489

490

491

492

493

Figure 17. Correct identification rates (blue triangles) of the four modulation formats with different launch powers in long-haul transmission experiments. Green dots indicate the error vector magnitudes (EVM).

The performance of the proposed scheme subject to nonlinear impairments of long-haul transmission links is experimentally explored and the results are presented in Figure 17, where the launch powers of the PDM-QPSK signals over a 2000 km link, the PDM-8QAM signals over a 2000 km link, the PDM-16QAM signals over a 1040 km link, and the PDM-32QAM signals over a 400 km link are varied in the ranges of -4~6dBm, -3~6dBm, -3~8dBm, and -2~7dBm, respectively. In Figure 17, EVM as a function of launch power are also plotted to evaluate the system overall performances of different modulation formats. Note that in comparison with other modulation formats, the EVM variation for 32QAM over the whole optical launch powers range is reduced, this is because of the relatively short link length. As seen in this figure, when the launch power is higher than 2 dBm, all the transmission systems operate at the nonlinear region where the system performance is dominated by fiber nonlinearity. Over such a region, the correct identification rates of 100% are still achievable for the four modulation formats. On the other hand, when launch powers are decreased to -4dBm and -3dBm for the PDM-QPSK and PDM-16QAM signals, respectively, as a direct result of the resulting reductions in OSNR, the correct identification rates for the PDM-QPSK and PDM-16QAM signals reduce with decreasing launch power. The experiment results indicate that the proposed MFI scheme is robust against fiber nonlinearities and suitable for long-haul transmission links.

5. Complexity analysis

To evaluate the feasibility of the proposed MFI algorithm for use in practical systems, its computational complexity has to be examined. The detailed complexity analysis of the proposed scheme is thus undertaken and the results are presented in Table 3, where the complexities of the five operations involved in the proposed MFI scheme are shown. For the proposed scheme, the required real multipliers, real adders and comparators are $N+6*(nbins+1)$, $N+7*nbins+6$ and $2*N+(2*N+10)*nbins+1$, respectively, here, N is the number of symbols (6000), and $nbins$ is the number of histogram bins (40).

Table 3. Computational complexity of the proposed MFI scheme

Operation	Multipliers	Adders	Comparators
Power normalization	N	$N-1$	0
Generation of amplitude histograms	0	$2*nbins$	$2*nbins*N+2*N-3$
Partition operation	0	$nbins-1$	$10*nbins$
Calculation of ratios	$6*(nbins+1)$	$4*nbins+8$	0
Comparing with threshold	0	0	4
Total	$N+6*(nbins+1)$	$N+7*nbins+6$	$2*N+(2*N+10)*nbins+1$

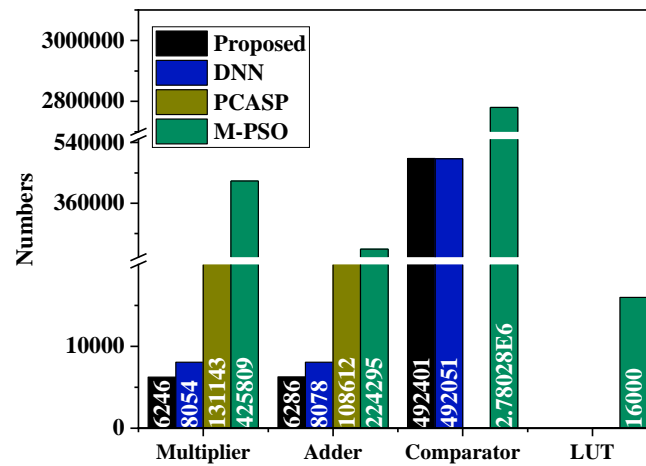


Figure 18. The complexity comparison between the proposed scheme and schemes using DNN, PCASP and M-PSO.

The complexity comparison between the proposed MFI scheme and schemes using DNN, PCASP and M-PSO is shown in Figure 18. Without considering the complexity of power normalization and amplitude histogram generation, in the testing stage of SVM, $O(N_s \cdot d \cdot N)$ operations are required when RBF kernel is applied [38], where N_s , d and N are the number of support vector, the dimension of the input data and the number of testing samples, respectively. Since the support vector cannot be fully quantified, the complexity of SVM is not considered in Figure 18. In the numerical simulations, N_s and d are 805 and 40, respectively. As shown in Figure 18, the required multiplications, additions and comparisons for M-PSO scheme are much higher than those of the proposed scheme. In addition, 16000 look-up table (LUT) operations are also required for M-PSO scheme. When the number of symbols N equals to 2048, the PCASP scheme needs calculations of 131143 real multiplications, 108612 real additions, 14 comparisons and 22 LUT operations. For the proposed scheme, the required real multiplications, real additions and comparisons are just 6246, 6286 and 492401, respectively. It should be noted that the complexity of the comparators is much lower than those related to multipliers and adders [29]. The proposed scheme and scheme using DNN are both based on amplitude histogram. Without considering the complexity of power normalization and amplitude histogram generation, the required real multipliers, real adders and comparators for the identification process in the proposed scheme are $6 \cdot (nbins+1)$, $5 \cdot nbins+7$ and $10 \cdot nbins+4$, respectively. The identification process in DNN, however, requires $N_1 N_2 + N_2 N_3 + N_3 N_4 + C - 1$ multipliers, $(N_1 - 1) N_2 + (N_2 - 1) N_3 + (N_3 - 1) N_4 + C - 1$ adders and $N_2 + N_3 + C - 1$ comparators, respectively [6], here N_1 , N_2 , N_3 and N_4 are the numbers of neurons in the input, first hidden, second hidden and output layer, respectively, and C is the number of identified modulation formats. In this paper, N_1 , N_2 , N_3 , N_4 and C are taken to be 40, 40, 10, 5 and 5, respectively. In addition, the training process of DNN and SVM may also require considerable computational resources and long processing time. Even though the training process can be accomplished offline, the training procedure is still regarded as a major factor limiting the flexibility of EONs.

6. Discussion

In Section 3, we had discussed the scalability of the proposed scheme. The precondition under which the proposed scheme can still identify PS-QAM is that the relevant statistical features of “to be identified” PS-QAM have to be constant. If the information entropy changes, the probability distribution features of PS-QAM also change. As such when PS-QAM with different information entropy needs to be identified, corresponding modifications to the procedure of the proposed MFI scheme and their relevant thresholds must be made. The proposed scheme is suitable for application scenarios where the set of

the modulation formats that needs to be identified from are made known before applying the MFI scheme. The authors would like to highlight the fact that such a condition also holds for machine learning MFI algorithms, since they also need training samples to contain the “to be identified” modulation formats in their training process. In other words, if the modulation formats of an incoming signal are not made known before the training process is applied, the machine learning algorithm will also fail to work properly. Furthermore, the proposed scheme can not identify higher-order modulation formats, such as 128QAM and 256QAM, because of the low tolerance to noise. Under the influence of noise, the corresponding amplitude features of these higher-order modulation formats are not highlighted in histogram, and result in increased difficulty of identification. How to identify the higher-order modulation formats is the work we need to explore next.

7. Conclusions

In this paper, a MFI scheme based on amplitude histogram distributions has been proposed for use in autonomous digital coherent receivers in EONs. The feasibility of the proposed scheme has been verified by numerical simulations for 28GBaud PDM-QPSK/-8QAM/-16QAM/-32QAM/-64QAM signals over a wide range of OSNRs. Following the numerical simulations, to further demonstrate the effectiveness of the proposed scheme, proof-of-concept experiments have also been undertaken in 28GBaud PDM-QPSK/-8QAM/-16QAM, and 21.5GBaud PDM-32QAM systems under back-to-back and long-haul fiber transmission links. Simulation and experiment results have shown that the proposed scheme is robust against both linear and nonlinear noises. Equally importantly, such performances are obtained with significantly reduced complexity. The proposed scheme is dependent on amplitude features only, thus insensitive to carrier phase noise. In addition, the proposed MFI scheme is also capable of identifying PS-QAM signals when slight modifications to the procedure and corresponding thresholds are made. According to the tradeoff between the identification performance and computational complexity, the proposed MFI scheme may have good potential for implementation in future EONs.

Author Contributions: Conceptualization, M.H. and X.D.J.; methodology, M.H., X.D.J., X.Z.X. and J.M.T.; software, M.H., X.D.J. and W.H.; validation, M.H. and X.D.J.; formal analysis, M.H., X.D.J. and J.M.T.; writing—original draft preparation, M.H. and X.D.J.; writing—review and editing, J.M.T. and R.G.; supervision, J.M.T., R.G. and X.Z.X.; project administration, M.H., J.M.T. and R.G.; funding acquisition, M.H., J.M.T. and R.G. All authors have read and agreed to the published version of the manuscript.

Funding: This research was partly supported by the [Sichuan Science and Technology Program \(2023YFH0067\)](#), the DSP Centre funded by the European Regional Development Fund through Welsh Government and also by the North Wales Growth Deal through Ambition North Wales, Welsh Government and UK Government, and the Opening Project of Key Laboratory of Higher Education of Sichuan Province for Enterprise Informationalization and Internet of Things (2021WYJ03).

Acknowledgement: This work was supported by the program of China Scholarship Council (No. 202008515061) and the Innovation Fund of Postgraduate, Sichuan University of Science & Engineering (y2021070).

Informed Consent Statement: Not applicable.

Data Availability Statement: Data underlying the results presented in this paper are not publicly available at this time but may be obtained from the authors upon reasonable request.

Conflicts of Interest: The authors declare no conflicts of interest.

References

1. O. Gerstel, M. Jinno, A. Lord, and S. J. B. Yoo, "Elastic optical networking: a new dawn for the optical layer?," *IEEE Commun. Mag.* **50**(2), s12-s20 (2012). 610 611
2. J. Feng, L. Jiang, L. Yan, A. Yi, W. Pan, and B. Luo, "Intelligent Optical Performance Monitoring Based on Intensity and Differential-Phase Features for Digital Coherent Receivers," *J. Lightwave Technol.* **40**(12), 3592-3601 (2022). 612 613
3. Y. Zhao, Z. Yu, Z. Wan, S. Hu, L. Shu, J. Zhang, and K. Xu, "Low Complexity OSNR Monitoring and Modulation Format Identification Based on Binarized Neural Networks," *J. Lightwave Technol.* **38**(6), 1314-1322 (2020). 614 615
4. L. Zhao, H. Xu, S. Bai, and C. Bai, "Modulus mean square-based blind hybrid modulation format recognition for orthogonal frequency division multiplexing-based elastic optical networking," *Opt. Commun.* **445**, 284-290 (2019). 616 617
5. L. Jiang, L. Yan, A. Yi, Y. Pan, M. Hao, W. Pan, and B. Luo, "Blind optical modulation format identification assisted by signal intensity fluctuation for autonomous digital coherent receivers," *Opt. Express* **28**(1), 302-313 (2020). 618 619
6. Y. Zhao, C. Shi, D. Wang, X. Chen, L. Wang, T. Yang, and J. Du, "Low-Complexity and Nonlinearity-Tolerant Modulation Format Identification Using Random Forest," *IEEE Photonics Technol. Lett.* **31**(11), 853-856 (2019). 620 621
7. L. Yang, H. Xu, C. Bai, X. Yu, K. You, W. Sun, J. Guo, X. Zhang, and C. Liu, "Modulation Format Identification Using Graph-Based 2D Stokes Plane Analysis for Elastic Optical Network," *IEEE Photonics J.* **13**(1), 7901315 (2021). 622 623
8. H. Xu, L. Yang, X. Yu, Z. Zheng, C. Bai, W. Sun, and X. Zhang, "Blind and low-complexity modulation format identification scheme using principal component analysis of Stokes parameters for elastic optical networks," *Opt. Express* **28**(14), 20249-20263 (2020). 624 625 626
9. M. Xiang, Q. Zhuge, M. Qiu, X. Zhou, F. Zhang, M. Tang, D. Liu, S. Fu, and D. V. Plant, "Modulation format identification aided hitless flexible coherent transceiver," *Opt. Express* **24**(14), 15642-15655 (2016). 627 628
10. M. Xiang, Q. Zhuge, M. Qiu, X. Zhou, M. Tang, D. Liu, S. Fu, and D. V. Plant, "RF-pilot aided modulation format identification for hitless coherent transceiver," *Opt. Express* **25**(1), 463-471 (2017). 629 630
11. S. Fu, Z. Xu, J. Lu, H. Jiang, Q. Wu, Z. Hu, M. Tang, D. Liu, and C. C. Chan, "Modulation format identification enabled by the digital frequency-offset loading technique for hitless coherent transceiver," *Opt. Express* **26**(6), 7288-7296 (2018). 631 632
12. R. Borkowski, D. Zibar, A. Caballero, V. Arlunno, and I. T. Monroy, "Stokes Space-Based Optical Modulation Format Recognition for Digital Coherent Receivers," *IEEE Photonics Technol. Lett.* **25**(21), 2129-2132 (2013). 633 634
13. P. Chen, J. Liu, X. Wu, K. Zhong, and X. Mai, "Subtraction-Clustering-Based Modulation Format Identification in Stokes Space," *IEEE Photonics Technol. Lett.* **29**(17), 1439-1442 (2017). 635 636
14. X. Mai, J. Liu, X. Wu, Q. Zhang, C. Guo, Y. Yang, and Z. Li, "Stokes space modulation format classification based on non-iterative clustering algorithm for coherent optical receivers," *Opt. Express* **25**(3), 2038-2050 (2017). 637 638
15. M. Hao, L. Yan, A. Yi, L. Jiang, Y. Pan, W. Pan, and B. Luo, "Stokes Space Modulation Format Identification for Optical Signals Using Probabilistic Neural Network," *IEEE Photonics J.* **10**(3), 7202213 (2018). 639 640
16. L. Jiang, L. Yan, A. Yi, Y. Pan, T. Bo, M. Hao, W. Pan, and B. Luo, "Blind Density-Peak-Based Modulation Format Identification for Elastic Optical Networks," *J. Lightwave Technol.* **36**(14), 2850-2858 (2018). 641 642
17. W. Zhang, D. Zhu, Z. He, N. Zhang, X. Zhang, H. Zhang, and Y. Li, "Identifying modulation formats through 2D Stokes planes with deep neural networks," *Opt. Express* **26**(18), 23507-23517 (2018). 643 644
18. A. Yi, L. Yan, H. Liu, L. Jiang, Y. Pan, B. Luo, and W. Pan, "Modulation format identification and OSNR monitoring using density distributions in Stokes axes for digital coherent receivers," *Opt. Express* **27**(4), 4471-4479 (2019). 645 646
19. H. J. Cho, S. Varughese, D. Lippiatt, R. Desalvo, S. Tibuleac, and S. E. Ralph, "Optical performance monitoring using digital coherent receivers and convolutional neural networks," *Opt. Express* **28**(21), 32087-32104 (2020). 647 648
20. X. Yu, C. Bai, H. Xu, W. Sun, L. Yang, H. Zheng, and W. Hu, "A modified PSO assisted blind modulation format identification scheme for elastic optical networks," *Opt. Commun.* **476**, 126280-126290 (2020). 649 650
21. M. Wang, J. Liu, J. Zhang, D. Zhang, and C. Guo, "Modulation format identification based on phase statistics in Stokes space," 651

- Opt. Commun. **480**, 126481-126487 (2021). 652
22. Q. Xiang, Y. Yang, Q. Zhang, and Y. Yao, "Joint, accurate and robust optical signal-to- noise ratio and modulation format monitoring scheme using a single Stokes-parameter-based artificial neural network," Opt. Express **29**(5), 7276-7287 (2021). 653
 23. R. Zhao, W. Sun, H. Xu, C. Bai, X. Tang, Z. Wang, L. Yang, L. Cao, Y. Bi, X. Yu, W. Fang, B. Li, T. Zhou, and P. Ge, "Blind modulation format identification based on improved PSO clustering in a 2D Stokes plane," Appl. Opt. **60**(31), 9933-9942 (2021). 654
 24. J. Liu, Z. Dong, K. Zhong, A. P. T. Lau, C. Lu, and Y. Lu, "Modulation format identification based on received signal power distributions for digital coherent receivers," in *Optical Fiber Communication Conference*, (Optical Society of America, 2014), Th4D. 655
 3. 656
 25. S. M. Bilal, G. Bosco, Z. Dong, A. P. Lau, and C. Lu, "Blind modulation format identification for digital coherent receivers," Opt. Express **23**(20), 26769-26778 (2015). 657
 26. X. Lin, Y. A. Eldemerdash, O. A. Dobre, S. Zhang, and C. Li, "Modulation Classification Using Received Signal's Amplitude Distribution for Coherent Receivers," IEEE Photonics Technol. Lett. **29**(21), 1872-1875 (2017). 658
 27. G. Liu, R. Proietti, K. Zhang, H. Lu, and S. J. Ben Yoo, "Blind modulation format identification using nonlinear power transformation," Opt. Express **25**(25), 30895-30904 (2017). 659
 28. L. Jiang, L. Yan, A. Yi, Y. Pan, M. Hao, W. Pan, and B. Luo, "An Effective Modulation Format Identification Based on Intensity Profile Features for Digital Coherent Receivers," J. Lightwave Technol. **37**(19), 5067-5075 (2019). 660
 29. J. Lu, Z. Tan, A. P. T. Lau, S. Fu, M. Tang, and C. Lu, "Modulation format identification assisted by sparse-fast-Fourier-transform for hitless flexible coherent transceivers," Opt. Express **27**(5), 7072-7086 (2019). 661
 30. Z. Zhao, A. Yang, and P. Guo, "A Modulation Format Identification Method Based on Information Entropy Analysis of Received Optical Communication Signal," IEEE Access **7**, 41492-41497 (2019). 662
 31. Z. Zhao, A. Yang, P. Guo, Q. Tan, and X. Xin, "A modulation format identification method based signal amplitude sorting and ratio calculation," Opt. Commun. **470**, 125819-125825 (2020). 663
 32. L. Yang, H. Xu, C. Bai, X. Yu, K. You, W. Sun, X. Zhang, and C. Liu, "Low-complexity modulation format identification scheme via graph-theory in digital coherent optical receivers," Opt. Commun. **501**, 127380-127387 (2021). 664
 33. L. Yang, H. Xu, C. Bai, X. Yu, P. Ge, K. You, W. Sun, X. Zhang, and C. Liu, "Joint modulation format identification and OSNR estimation method based on trajectory information analysis," Opt. Commun. **507**, 127657-127668 (2022). 665
 34. F. N. Khan, K. Zhong, W. H. Al-Arashi, C. Yu, C. Lu, and A. P. T. Lau, "Modulation Format Identification in Coherent Receivers Using Deep Machine Learning," IEEE Photonics Technol. Lett. **28**(17), 1886-1889 (2016). 666
 35. F. N. Khan, K. Zhong, X. Zhou, W. H. Al-Arashi, C. Yu, C. Lu, and A. P. T. Lau, "Joint OSNR monitoring and modulation format identification in digital coherent receivers using deep neural networks," Opt. Express **25**(15), 17767-17776 (2017). 667
 36. T. Wang and X. Liu, "A novel modulation format identification based on amplitude histogram space," Front. Optoelectron. **12**(2), 190-196 (2019). 668
 37. C. Zhu, A. V. Tran, S. Chen, L. B. Du, C. C. Do, T. Anderson, A. J. Lowery, and E. Skafidas, "Statistical moments-based OSNR monitoring for coherent optical systems," Opt. Express **20**(16), 17711-17721 (2012). 669
 38. X. Lin, O. A. Dobre, T. M. N. Ngatched, Y. A. Eldemerdash, and C. Li, "Joint Modulation Classification and OSNR Estimation Enabled by Support Vector Machine," IEEE Photonics Technol. Lett. **30**(24), 2127-2130 (2018). 670